AGU PUBLICATIONS

JGR

Journal of Geophysical Research: Space Physics

RESEARCH ARTICLE

10.1002/2013JA018982

Key Points:
- The inductive-dynamic approach is used to investigate M-I coupling
- Wave reflection and Hall effect are inherent aspects of the M-I coupling
- Wave heating may generate compressional waves

Correspondence to:
J. Tu,
Jiannan_Tu@uml.edu

Citation:
Tu, J., P. Song, and V. M. Vasyliūnas (2014), Inductive-dynamic magnetosphere-ionosphere coupling via MHD waves, *J. Geophys. Res. Space Physics*, *119*, 530–547, doi:10.1002/2013JA018982.

Received 24 APR 2013
Accepted 26 DEC 2013
Accepted article online 2 JAN 2014
Published online 23 JAN 2014

Inductive-dynamic magnetosphere-ionosphere coupling via MHD waves

Jiannan Tu[1], Paul Song[1], and Vytenis M. Vasyliūnas[1,2]

[1]Center for Atmospheric Research and Physics Department, University of Massachusetts, Lowell, Massachusetts, USA,
[2]Max-Planck-Institut für Sonnensystemforschung, Katlenburg-Lindau, Germany

Abstract In the present study, we investigate magnetosphere-ionosphere/thermosphere (M-IT) coupling via MHD waves by numerically solving time-dependent continuity, momentum, and energy equations for ions and neutrals, together with Maxwell's equations (Ampère's and Faraday's laws) and with photochemistry included. This inductive-dynamic approach we use is fundamentally different from those in previous magnetosphere-ionosphere (M-I) coupling models: all MHD wave modes are retained, and energy and momentum exchange between waves and plasma are incorporated into the governing equations, allowing a self-consistent examination of dynamic M-I coupling. Simulations, using an implicit numerical scheme, of the 1-D ionosphere/thermosphere system responding to an imposed convection velocity at the top boundary are presented to show how magnetosphere and ionosphere are coupled through Alfvén waves during the transient stage when the IT system changes from one quasi steady state to another. Wave reflection from the low-altitude ionosphere plays an essential role, causing overshoots and oscillations of ionospheric perturbations, and the dynamical Hall effect is an inherent aspect of the M-I coupling. The simulations demonstrate that the ionosphere/thermosphere responds to magnetospheric driving forces as a damped oscillator.

1. Introduction

Overshoots and oscillations of the ionospheric perturbations are routinely observed during substorms and other transient phenomena [e.g., *Russell and Ginskey*, 1993; *Bristow et al*., 2003; *Huang et al*., 2008]. The magnetosphere-ionosphere/thermosphere (M-IT) coupling models based on conventional ionospheric electrodynamics are not able to adequately model such dramatic variations because the conventional ionospheric electrodynamics (with magnetosphere-ionosphere (M-I) coupling through electric current closure, assuming a steady state ionospheric Ohm's law) is valid only for a quasi-steady but not a dynamic M-IT system [*Vasyliūnas*, 2012]. It has been shown by *Song et al*. [2009] and *Tu et al*. [2011] that an inductive-dynamic approach, which retains plasma/neutral dynamics and inductive effects, is necessary to correctly explain the overshoots and oscillations. In fact, coupling among different regions of space plasma occurs primarily via various waves, in addition to direct flows, given that any perturbation may be decomposed into a superposition of waves. On magnetohydrodynamic (MHD) time and spatial scales, the coupling between the magnetosphere and ionosphere and among different regions of the ionosphere is through either Alfvén waves propagating primarily along the magnetic field or compressional waves propagating oblique (primarily perpendicular) to the field. Collisions (e.g., between charged particles and neutrals) are local processes and do not directly provide long-range coupling. Collisions plus photochemical processes in the ionosphere/thermosphere (IT) do, however, affect wave propagation and reflection at low altitudes [e.g., *Song et al*., 2005a, 2005b]. In order to correctly understand magnetosphere-ionosphere/thermosphere (M-IT) coupling, one must, therefore, self-consistently solve time-dependent plasma and neutral continuity, momentum, and energy equations, together with Maxwell's equations that include the inductive term in Faraday's law and with collisional and photochemical processes.

The global MHD simulation models for the magnetosphere retain inductive effects and plasma dynamics in the magnetosphere. The coupling to the ionosphere, however, is assumed to be governed by the conventional steady state ionospheric Ohm's law, with the ionosphere treated as a height-integrated layer [e.g., *Walker et al*., 1993; *Fedder and Lyon*, 1995; *Janhunen*, 1996; *Raeder et al*., 1998; *Gombosi et al*., 1998; *Song et al*., 1999]. The only exception is the Integrated Space Weather Prediction (ISM) model [*White et al*., 1998; *Siscoe et al*., 2002] which attempted to model the magnetosphere-ionosphere/thermosphere as a unified system, but so far the ionosphere/thermosphere has not been well incorporated. A height-integrated ionosphere has also been assumed in many wave analysis models [e.g., *Lighthill*, 1960; *Lysak and Dum*, 1983; *Glaßmeier*, 1983; *Kivelson and Southwood*, 1988; *Yoshikawa and Itonaga*, 2000; *Lysak and Song*, 2002; *Lysak*, 1991, 2004; *Yoshikawa et al.*, 2011], but wave propagation and reflection obviously cannot be resolved within the ionosphere if the latter is treated as just a thin height-integrated layer.

Most of the global ionospheric/thermospheric models, on the other hand, neglect the inductive term in Faraday's law and the dynamical (time-derivative and convective) terms in the ion and electron momentum equations. As a result, the models become electrostatic. An often overlooked key point is that such a scheme describes only "quasi steady state" M-IT coupling and cannot be applied to explain transient processes, such as substorms and auroral brightening, during which the effects of magnetic perturbations are not negligibly small [*Song et al.*, 2009; *Tu et al.*, 2011; *Vasyliūnas*, 2012]. These models [e.g., *Richmond et al.*, 1992; *Fuller-Rowell et al.*, 1996; *Ridley et al.*, 2006] describe well the large-scale slow variations or "climatology" of the ionosphere/thermosphere system but not the rapidly changing phenomenon or its "weather" [*Schunk*, 2011]. Many other ionospheric models also assume the electrostatic condition [e.g., *Doe et al.*, 1995; *Huba et al.*, 2000; *De Boer et al.*, 2010; *Fujii et al.*, 2011] and thus do not contain any MHD wave effects.

A number of ionospheric models do include inductive effects within a structured ionosphere. For example, *Hughes* [1974] treated time-dependent phenomena as waves, using Fourier analysis. This approach retains propagation and reflection effects within the ionosphere but does not describe explicitly the plasma and neutral dynamics of the M-IT system. The ionospheric model of *Streltsov and Lotko* [2008] retains inductive effects of the parallel electric field but does not solve the energy equations (so that energy exchange between waves and plasma, such as wave heating, is absent), nor does it explicitly include neutral dynamics. The models of *Birk and Otto* [1996], *Zhu et al.* [2001], and *Otto et al.* [2003] incorporated both plasma and neutral dynamics/thermal dynamics; nevertheless, the interpretation of simulation results is still in the context of the conventional quasi steady state assumption. The models of *Lysak* [2004], *Woodroffe and Lysak* [2012], and *Lysak et al.* [2013] have been developed to model ULF wave propagation in the structure-resolved ionosphere, which includes the inductive effects, but the ionosphere is described by steady state Pedersen and Hall conductances.

The inductive-dynamic approach that we have developed differs from previous studies: we retain inductive effects, dynamics, and thermal dynamics of both plasma and neutrals, coupled with electromagnetic waves within the vertically structured ionosphere/thermosphere [*Song et al.*, 2009; *Tu et al.*, 2011]. In the present study we extend our previous simulations by incorporating continuity and energy equations of plasma and neutrals (in terms of plasma and neutral pressures) while still retaining the approximation of a one-dimensional ionosphere/thermosphere. By including time-derivative and advection terms in the plasma and neutral momentum equations and solving Maxwell's equations, thus keeping MHD waves of all modes, we can self-consistently investigate the dynamic M-I coupling. By adding the continuity and energy equations, we can investigate the mutual interaction of MHD waves with plasma self-consistently and more comprehensively. In the next section we describe the simulation model used in the present study. We discuss the implicit numerical scheme used to solve the governing equations in section 3. We present the simulation results, which resemble the observed oscillations and overshoots of ionospheric perturbations, in section 4 and a summary with discussion in section 5.

2. Simulation Model

2.1. Governing Equations

In the present study we consider a 1-D ionosphere/thermosphere, with all the quantities (densities, velocities, pressures, and perturbation magnetic field) varying spatially only along the vertical (z) direction, and a constant background magnetic field $\mathbf{B}_0 = -B_0\hat{\mathbf{z}}$. The velocities and the perturbation magnetic field may have components in any direction. The total magnetic field is $\mathbf{B} = \mathbf{B}_0 + \mathbf{B}_\perp$, where $\mathbf{B}_\perp$ is the perturbation magnetic field, which is perpendicular to the background magnetic field in the assumed 1-D geometry as a consequence of $\nabla \cdot \mathbf{B} = 0$. Note that this 1-D model cannot describe the horizontal coupling of different regions (which we intend to investigate after we understand how the magnetosphere and the ionosphere are coupled vertically).

The plasma and the neutral mass continuity equations are given by mass-weighted sums of the continuity equations for individual species, separately for charged and neutral species:

$$\frac{\partial \rho}{\partial t} + \frac{\partial(\rho V_z)}{\partial z} = S_m - \rho L_m \quad (1)$$

$$\frac{\partial \rho_n}{\partial t} + \frac{\partial(\rho_n U_z)}{\partial z} = \rho L_m - S_m \quad (2)$$

where ρ and ρ_n are the mass densities; V_z and U_z are vertical components of the bulk velocity for plasma and neutrals, respectively; S_m is the plasma mass production rate; and L_m is the plasma mass loss coefficient. The production and loss terms on the right-hand sides are in a form that ensures the conservation of total mass (plasma and neutrals). S_m is determined by photoionization and chemical reaction processes and L_m by chemical reaction processes. The procedure of calculating S_m and L_m is discussed in section 2.3.

The momentum equation for the entire plasma is obtained by summing the momentum equations of all the charged particles [e.g., *Schunk and Nagy*, 2000; *Song et al.*, 2005a]. For the assumed 1-D geometry, the components of the plasma momentum equation perpendicular and parallel to the magnetic field become

$$\frac{\partial \rho \mathbf{V}_\perp}{\partial t} + \frac{\partial \rho \mathbf{V}_\perp V_z}{\partial z} = \mathbf{J}_\perp \times \mathbf{B}_0 - \rho \nu_{in}(\mathbf{V}_\perp - \mathbf{U}_\perp) + \frac{m_e}{e}(\nu_{en} - \nu_{in})\mathbf{J}_\perp + S_m \mathbf{U}_\perp - \rho L_m \mathbf{V}_\perp \quad (3)$$

$$\frac{\partial \rho V_z}{\partial t} + \frac{\partial \rho V_z^2}{\partial z} + \frac{\partial P}{\partial z} = \mathbf{J}_\perp \times \mathbf{B}_\perp - \rho \nu_{in}(V_z - U_z) - \rho g + S_m U_z - \rho L_m V_z \quad (4)$$

where $\mathbf{V}_\perp$ and $\mathbf{U}_\perp$ are the plasma and neutral bulk velocities perpendicular to the background magnetic field (two components), respectively; V_z and U_z are vertical (field-aligned) component of the plasma and neutral bulk velocities, respectively; P is the plasma thermal pressure; $\mathbf{J}_\perp$ is the electric current density perpendicular to the background magnetic field; e is the elementary charge; m_e is the electron mass; ν_{in} and ν_{en} are the ion-neutral and electron-neutral collision frequencies, respectively; and g is the Earth's gravitational acceleration. Note that for the assumed 1-D geometry, $\hat{\mathbf{z}} \cdot \nabla \times \mathbf{B} = 0$; hence, locally there are no field-aligned currents, i.e., $J_\parallel = 0$. Similarly, the momentum equation for the entire neutral medium is

$$\frac{\partial \rho_n \mathbf{U}_\perp}{\partial t} + \frac{\partial \rho_n \mathbf{U}_\perp U_z}{\partial z} = \rho \nu_{in}(\mathbf{V}_\perp - \mathbf{U}_\perp) - \frac{m_e}{e}(\nu_{en} - \nu_{in})\mathbf{J}_\perp - S_m \mathbf{U}_\perp + \rho L_m \mathbf{V}_\perp \quad (5)$$

$$\frac{\partial \rho_n U_z}{\partial t} + \frac{\partial \rho_n U_z^2}{\partial z} + \frac{\partial P_n}{\partial z} = \rho \nu_{in}(V_z - U_z) - \rho_n g - S_m U_z + \rho L_m V_z \quad (6)$$

where P_n is the neutral thermal pressure. The last two terms on the right hand of (3)–(6) account for the momentum change due to production and loss of plasma, which in general is very small in comparison to that due to other processes included in the equations (these terms have opposite signs in the neutral and in the plasma momentum equations, so that the total momentum is always conserved).

To obtain the thermal pressures, plasma and neutral thermal pressure equations are needed. In this study we use the dissipation equations derived in *Vasyliūnas and Song* [2005] to evaluate pressures (assumed isotropic)

$$\frac{3}{2} P \frac{\mathrm{d}}{\mathrm{d}t}\left[\log\left(\frac{P}{\rho^{5/3}}\right)\right] = \mathbf{J}_\perp \cdot (\mathbf{E}_\perp + \mathbf{V} \times \mathbf{B}) + \frac{1}{2}\rho \nu_{in}(\mathbf{V} - \mathbf{U})^2 + \frac{1}{2}\rho \nu_{in} \xi \left(w_n^2 - w^2\right) - \frac{\partial q}{\partial z} + Q_p \quad (7)$$

$$\frac{3}{2} P_n \frac{\mathrm{d}}{\mathrm{d}t}\left[\log\left(\frac{P_n}{\rho_n^{5/3}}\right)\right] = \frac{1}{2}\rho \nu_{in}(\mathbf{V} - \mathbf{U})^2 - \frac{1}{2}\rho \nu_{in} \xi (w_n^2 - w^2) - \frac{\partial q_n}{\partial z} + Q_n - C_n \quad (8)$$

where w_n and w are the neutral and plasma thermal velocities, respectively; ξ is a constant with a value of ~ 1 [*Vasyliūnas and Song*, 2005], which is set to 1. Added to the equations as given by *Vasyliūnas and Song* [2005] are terms associated with plasma and neutral heat flux q and q_n, additional plasma heating Q_p, and neutral heating due to solar radiation Q_n, as well as neutral radiation cooling rate C_n. In the present study we simply assume Q_n is balanced by C_n, i.e., $Q_n - C_n = 0$. The plasma and neutral heat fluxes are calculated using formula given by *Banks and Kockarts* [1973]. The photoelectron heating rate given by *Millward et al.* [1996] for direct photoelectron heating of thermal electrons is adapted by assuming that the heat is deposited in the entire plasma.

The first term on the right hand of (7) represents true Joule heating ($\mathbf{E} \cdot \mathbf{J}$ in the plasma frame of reference). The second term is frictional heating caused by ion-neutral collisions, which is much stronger than true Joule heating except at altitudes below 100 km [*Vasyliūnas and Song*, 2005; *Tu et al.*, 2011]. The third term is heat transfer between plasma and neutrals when their thermal velocities are different. The thermal velocity of plasma is defined by $w^2 = 2k_B T/\bar{m}$, where k_B is Boltzmann constant, and T and $\bar{m}$ are the temperature and the mean particle mass of the plasma, respectively. From the relation $P = n_e k_B T$, where n_e is the electron number density, we have $w^2 = 2n_e k_B T/n_e \bar{m} = 2P/\rho$. A similar expression holds for the neutral thermal velocity. Therefore, we can write the third term on the right hand of (7) (and the second term on the right hand of (8)) as

$$\frac{1}{2}\rho \nu_{in}\xi(w_n^2 - w^2) = \rho \nu_{in}\xi \left(\frac{P_n}{\rho_n} - \frac{P}{\rho}\right) \tag{9}$$

We also need Maxwell's equations if we are to include MHD waves,

$$\frac{\partial \mathbf{B}_\perp}{\partial t} = -\hat{\mathbf{z}} \times \frac{\partial \mathbf{E}_\perp}{\partial z} \tag{10}$$

$$\mu_0 \mathbf{J}_\perp = \hat{\mathbf{z}} \times \frac{\partial \mathbf{B}_\perp}{\partial z} \tag{11}$$

where we have neglected the displacement current term since we only consider low-frequency phenomena. The electric field $\mathbf{E}_\perp$ is evaluated from the generalized Ohm's law with electron inertia terms neglected [e.g., *Vasyliūnas and Song*, 2005], giving in the assumed 1-D geometry

$$\mathbf{E}_\perp = -(\mathbf{V}_z \times \mathbf{B}_\perp + \mathbf{V}_\perp \times \mathbf{B}_0) + \frac{1}{en_e}\mathbf{J}_\perp \times \mathbf{B}_0 + \eta \mathbf{J}_\perp \tag{12}$$

where the resistivity $\eta = m_e(\nu_{en} + \nu_{ei})/e^2 n_e$ with ν_{ei} the electron-ion collision frequency.

For simplicity, we calculate the electron density used to derive the resistivity by using quasi-neutrality $n_e = \rho/\bar{m}$, where the mean plasma particle mass $\bar{m}$ is determined initially by the densities of various ion species calculated from the International Reference Ionosphere (IRI2011) [*Bilitza et al.*, 2011]. Since we treat the plasma as a single fluid and do not follow the temporal evolution of mass density for individual ion species, we cannot update $\bar{m}$ and must keep it constant at its initial value. The simulation thus describes the evolution of the M-IT system only for a limited period of time, before vertical plasma transport has changed the ion compositions appreciably. From the continuity equation (1), we can determine the order of magnitude of the time scale, Δt, during which $\partial \bar{m}/\partial t$ is negligibly small compared to other terms. Inserting $\rho = n_e \bar{m}$ into (1), we have $\Delta t \sim \Delta z/V_z$ or, taking $\Delta z = 1000$ km and vertical transport velocity $V_z = 1$ km/s, $\Delta t \sim 1000$ s. This time period, during which M-IT coupling is dominated by dynamic rather than by aeronomic effects, is the focus of our study.

In the present simulations we represent the M-IT system by a small-size model only 920 km in altitude (80–1000 km). The calculated time scales of interest are shortened accordingly and range from several seconds to several tens of seconds, as shown in section 4, because the propagation time of the Alfvén waves (or Alfvén travel time) is about half a second for such small distances. With the M-IT system given its real size, if the driving force is at the magnetopause, about 10 R_E away from the ionosphere, the Alfvén travel time is of the order 100 s and the time scales, e.g., for the ionosphere to change from one quasi steady state to another, become the order of tens of minutes.

2.2. Boundary Conditions

At the bottom boundary ($z = 80$ km), it is assumed that transport effects are negligibly small; hence, the plasma and neutral mass densities are determined by production and loss processes

$$\frac{\partial \rho}{\partial t} = S_m - \rho L_m \tag{13}$$

$$\frac{\partial \rho_n}{\partial t} = \rho L_m - S_m \tag{14}$$

The horizontal velocity components of the plasma, $\mathbf{V}_\perp$, and neutral, $\mathbf{U}_\perp$, are set to 0 at the lower boundary. The vertical (z) velocity component is also assumed 0 at the lower boundary in principle; in the simulation, however, the vertical velocities are defined at half grid indexes $j + 1/2$ ($j = 0, 1, 2, \ldots, N$, where N is the number of spatial cells; see section 3 for more detailed discussion), so that we need to specify the values for V_z and U_z at the index $-1/2$ (half grid below the lower boundary) and set $V_{z,-1/2} = U_{z,-1/2} = 0$. The pressures at the lower boundary are simply kept at their initial values, calculated by using plasma and neutral densities and temperatures from the IRI2011 model and NRLMSISE00 empirical thermospheric model [*Picone et al.*, 2002]. Test runs (data not shown) have shown that the simulation results are not sensitive to the lower boundary conditions for densities, velocities, and pressures. This is reasonable because of strong collisions at 80 km, which makes plasma and neutral barely move in response to driving forces from the top boundary. For the perturbation magnetic field, either $\mathbf{B}_\perp = 0$ or $\partial \mathbf{B}_\perp/\partial z = 0$ (equivalent to $\mathbf{J}_\perp = 0$) may be considered as reasonable boundary conditions at the bottom of the ionosphere, which can be regarded as the interface between the conducting ionosphere and the atmosphere that is effectively nonconducting (although not a perfect insulator in reality). We tested both possible boundary conditions, with the result that, while the detailed values are different for the two, the basic features of interest, such as overshooting and oscillations in the velocities, pressures, and perturbation magnetic field (as shown in section 4) are found in the simulation with either one. In this paper we present results only for the simulation with boundary condition $\mathbf{B}_\perp = 0$ at $z = 80$ km.

At the top boundary (1000 km), we impose open boundary conditions (i.e., the spatial derivative of densities, velocities, pressures, and perturbation magnetic field are 0) besides the imposed antisunward convection velocity V_x. Note that we simulate a scaled M-IT system with the top boundary only at 1000 km. The V_x is specified as the driving source similar to that at the magnetopause. We have also tested other boundary conditions at the top, such as linear extrapolation of the densities, velocities (other than the specified V_x), and pressures, and have found that simulations results are essentially the same, but for long-time runs simulations are more stable with open boundary conditions.

2.3. Photoionization and Chemical Reactions

The production rate S_m and the loss coefficient L_m in the continuity equations (1) and (2) are determined by ion production and loss processes. Ions are produced by photoionization of neutrals and by chemical reactions of ions with neutrals; the latter are also responsible for loss of ions in the reactions.

The photoionization rate of neutral species s is given by [e.g., *Schunk and Nagy*, 2000]

$$p_s(z) = n_s(z) \sum_\lambda \sigma_s^i(\lambda) F(\lambda) \exp\left[-\sum_r \sigma_r^a(\lambda) \int_z^\infty n_r(l)\mathrm{d}l\right] \tag{15}$$

where $p_s(z)$ is the photoionization rate of neutral species s at altitude z; n_s and n_r are the densities of neutral species s and r, respectively; $F(\lambda)$ is the incident solar EUV flux at wavelength λ; and $\sigma_s^i(\lambda)$ and $\sigma_r^a(\lambda)$ are the ionization and photoabsorption cross sections, respectively, of species s at λ. The integral $\int_z^\infty n_r(l)\mathrm{d}l$ is evaluated along a ray from the sun to the observation point at altitude z. We use the method developed by *Smith and Smith* [1972] to calculate the integral, which is based on an exponential atmosphere and is generally accurate enough when the solar zenith angle $\chi \neq 90°$. The incident solar EUV flux is calculated from the solar EUV flux model for aeronomic calculations developed by *Richards et al.* [1994] which is based on a reference flux F74113 in 37 bins of the wavelength

$$F(\lambda_i) = F74113_i\{1 + A_i[(F107 + F107A)/2 - 80]\},\ i = 1, 2, \ldots, 37 \tag{16}$$

where F107 is 10.7 cm solar flux and F107A is its 81 day average (centered at the date of F107). The values of $F73113_i$ and A_i for 37 wavelength bins from 50 to 1050 Å, along with the photoabsorption and photoionization cross sections in the 37 bins for various neutral species, are given in *Richards et al.* [1994]. In our simulations we calculate photoionization rates for N, O, He, N_2, and O_2 from (15). The densities of N, O, He, N_2, and O_2 are determined by the empirical thermospheric model NRLMSISE00. In addition, using the same method in *Huba et al.* [2000], we also include nighttime photoionization due to starlight (stellar continuum radiation in the spectral interval 911–1026 A) and resonance scattering of solar $Ly-\alpha$ and $Ly-\beta$ into the night sector, which are important to maintain the nighttime E region of the ionosphere.

Besides photoionization, charge exchange or dissociative reactions change ion species from one to another so that the mean plasma particle mass is altered. We consider 21 reactions, listed in *Huba et al.* [2000].

An ion-electron pair may be lost through recombination. We consider seven recombination processes, namely, $O^+ + e \rightarrow O$, $H^+ + e \rightarrow H$, $He^+ + e \rightarrow He$, $NO^+ + e \rightarrow NO$, $N_2^+ + e \rightarrow N_2$, $N^+ + e \rightarrow N$, and $O_2^+ + e \rightarrow O_2$. The reaction rates of these recombination reactions are obtained from *Schunk and Nagy* [2000].

The plasma mass production rate and loss coefficient are thus defined as

$$S_m = \sum_s m_s p_s + \sum_s \sum_r m_s n_s n_r k_{r,s} \tag{17}$$

$$\rho L_m = \sum_r \sum_s m_r n_r n_s k_{r,s} + \sum_t m_t n_t n_e k_{r,e} \tag{18}$$

where m_s and n_s are the mass and number density of the neutral species s, respectively; $k_{r,s}$ is the reaction rate of ion species r with the neutral species s to produce the ion species s (and to cause the loss of ion species r); m_r and n_r are the mass and density of ion r, respectively, involved in the reaction; and $k_{r,e}$ is the recombination rate of the ion r with the electron. Those reaction rates are also taken from *Schunk and Nagy* [2000].

In the simulation model of the present study, the plasma and the neutrals are each treated as a single fluid so that the density and temperature of the individual ion species (as well as the individual neutral species) are not updated in time. The plasma mass production rate S_m and loss coefficient L_m therefore are held constant in the simulations and are calculated only at the initial time, with the density of the individual ion species and the ion and electron temperatures determined from the IRI2011 empirical model, and with the density of the individual neutral species and the neutral temperature determined from the NRLMSISE00 model. Although the limitation of unvarying density of individual neutral species and mean plasma particle mass $\bar{m}$ restricts the ability of our simulation model to adequately describe the corresponding ionospheric modifications, the model does yield a reasonable representation of ionospheric/thermospheric response to magnetospheric input during the transition period, similarly to models of *Birk and Otto* [1996] and *Dreher* [1997].

3. Numerical Scheme

By substituting the electric current density from Ampère's law (11) into (3)–(5) and into (7), and the electric field from the generalized Ohm's law (12) into (7) and (10), we obtain a set of nonlinear partial differential equations for plasma and neutral mass densities ρ and ρ_n, velocities $\mathbf{V}$ and $\mathbf{U}$, pressures P and P_n, and perturbation magnetic field $\mathbf{B}_\perp$. This equation set describes the dynamics of the plasma, neutrals, and magnetic field on MHD time scales for a self-consistent simple 1-D ionosphere/thermosphere, with Hall effect, collisional resistivity, plasma-neutral friction, and photochemistry included.

The nonlinear differential equations are discretized with a fully implicit difference method. We chose the fully implicit difference scheme instead of an explicit one in order to remove the strict restriction on the time step by the stiffness of the differential equations [*Tu et al.*, 2011]. The stiffness arises from terms containing the ion-neutral collision frequency ν_{in}, which is very large (up to 10^6 s^{-1}; see Figure 1) in the low-altitude ionosphere. The difference equations resulting from the fully implicit scheme, with normalized variables, are

$$\frac{\bar{\rho}_j^{n+1} - \bar{\rho}_j^n}{\Delta \bar{t}} + \frac{(\bar{\rho}\bar{V}_z)_{j+1/2}^{n+1} - (\bar{\rho}\bar{V}_z)_{j-1/2}^{n+1}}{\Delta \bar{z}} = \bar{S}_{m,j} - \bar{L}_{m,j}\bar{\rho}_j^{n+1} \tag{19}$$

$$\frac{\bar{\rho}_{n,j}^{n+1} - \bar{\rho}_{n,j}^n}{\Delta \bar{t}} + \frac{(\bar{\rho}_n\bar{U}_z)_{j+1/2}^{n+1} - (\bar{\rho}_n\bar{U}_z)_{j-1/2}^{n+1}}{\Delta \bar{z}} = \alpha(\bar{L}_{m,j}\bar{\rho}_j^{n+1} - \bar{S}_{m,j}) \tag{20}$$

$$\begin{aligned}\frac{(\bar{\rho}\bar{\mathbf{V}}_\perp)_j^{n+1} - (\bar{\rho}\bar{\mathbf{V}}_\perp)_j^n}{\Delta \bar{t}} &+ \frac{(\bar{V}_z\bar{\rho}\bar{\mathbf{V}}_\perp)_{j+1/2}^{n+1} - (\bar{V}_z\bar{\rho}\bar{\mathbf{V}}_\perp)_{j-1/2}^{n+1}}{\Delta \bar{z}} + \frac{\bar{\mathbf{B}}_{\perp,j+1}^{n+1} - \bar{\mathbf{B}}_{\perp,j-1}^{n+1}}{2\Delta \bar{z}} = -\bar{\rho}_j^{n+1}\bar{\nu}_{in,j}\left(\bar{\mathbf{V}}_{\perp,j}^{n+1} - \bar{\mathbf{U}}_{\perp,j}^{n+1}\right) \\ &+ \frac{(\bar{\nu}_{en,j} - \bar{\nu}_{in,j})}{\bar{\Omega}_e}\hat{\mathbf{z}} \times \frac{\bar{\mathbf{B}}_{\perp,j+1}^{n+1} - \bar{\mathbf{B}}_{\perp,j-1}^{n+1}}{2\Delta \bar{z}} + \bar{S}_{m,j}\bar{\mathbf{U}}_{\perp,j}^{n+1} - \bar{L}_{m,j}\bar{\rho}_j^{n+1}\bar{\mathbf{V}}_{\perp,j}^{n+1}\end{aligned} \tag{21}$$

$$\begin{aligned}\frac{(\bar{\rho}\bar{V}_z)_{j+1/2}^{n+1} - (\bar{\rho}\bar{V}_z)_{j+1/2}^n}{\Delta \bar{t}} &+ \frac{(\bar{V}_z^2\bar{\rho})_{j+1}^{n+1} - (\bar{V}_z^2\bar{\rho})_j^{n+1}}{\Delta \bar{z}} + \frac{\bar{P}_{j+1}^{n+1} - \bar{P}_j^{n+1}}{\Delta \bar{z}} + \frac{(\bar{B}^2)_{\perp,j+1}^{n+1} - (\bar{B}^2)_{\perp,j}^{n+1}}{2\Delta \bar{z}} \\ &= -\bar{\rho}_{j+1/2}^{n+1}\bar{\nu}_{in,j+1/2}(\bar{V}_{z,j+1/2}^{n+1} - \bar{U}_{z,j+1/2}^{n+1}) - \bar{\rho}_{j+1/2}^{n+1}\bar{g}_{j+1/2} + \bar{S}_{m,j+1/2}\bar{U}_{z,j+1/2}^{n+1} \\ &\quad - \bar{L}_{m,j+1/2}\bar{\rho}_{j+1/2}^{n+1}\bar{V}_{z,j+1/2}^{n+1}\end{aligned} \tag{22}$$

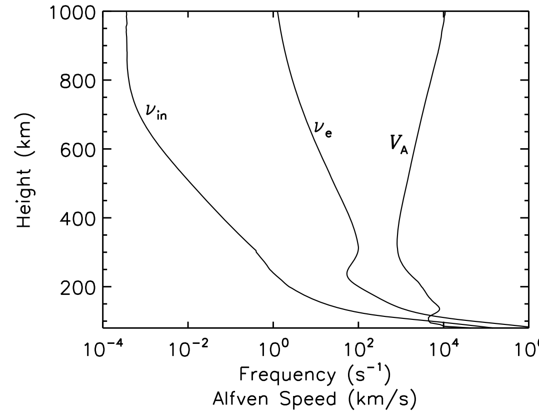

Figure 1. Altitude variation of Alfvén speed $V_A = \sqrt{B_0/\rho\mu_0}$ and ion-neutral and electron collision frequencies, ν_{in} and $\nu_e = \nu_{en} + \nu_{ei}$, calculated at the start of the simulation ($t = -120$ s).

$$\frac{(\bar\rho_n \bar{\mathbf U}_\perp)_j^{n+1} - (\bar\rho_n \bar{\mathbf U}_\perp)_j^n}{\Delta \bar t} + \frac{(\bar U_z \bar\rho_n \bar{\mathbf U}_\perp)_{j+1/2}^{n+1} - (\bar U_z\bar\rho_n\bar{\mathbf U}_\perp)_{j-1/2}^{n+1}}{\Delta\bar z} = \alpha\bar\rho_j^{n+1}\bar\nu_{in,j}\left(\bar{\mathbf V}_{\perp,j}^{n+1} - \bar{\mathbf U}_{\perp,j}^{n+1}\right) - \frac{\alpha(\bar\nu_{en,j}-\bar\nu_{in,j})}{\bar\Omega_e}\hat{\mathbf z}\times\frac{\bar{\mathbf B}_{\perp,j+1}^{n+1}-\bar{\mathbf B}_{\perp,j-1}^{n+1}}{2\Delta\bar z} + \alpha\left(\bar L_{m,j}\bar\rho_j^{n+1}\bar{\mathbf V}_{\perp,j}^{n+1} - \bar S_{m,j}\bar{\mathbf U}_{\perp,j}^{n+1}\right) \tag{23}$$

$$\frac{(\bar\rho_n \bar U_z)_{j+1/2}^{n+1} - (\bar\rho_n \bar U_z)_{j+1/2}^n}{\Delta \bar t} + \frac{\left(\bar U_z^2\bar\rho_n\right)_{j+1}^{n+1} - \left(\bar U_z^2\bar\rho_n\right)_j^{n+1}}{\Delta\bar z} + \frac{\bar p_{n,j+1}^{n+1} - \bar p_{n,j}^{n+1}}{\Delta\bar z} = \alpha\bar\rho_{j+1/2}^{n+1}\bar\nu_{in,j+1/2} \cdot\left(\bar V_{z,j+1/2}^{n+1} - \bar U_{z,j+1/2}^{n+1}\right) - \bar\rho_{n,j+1/2}^{n+1} g_{j+1/2} + \alpha\left(\bar L_{m,j+1/2}\bar\rho_{j+1/2}^{n+1}\bar V_{z,j+1/2}^{n+1} - \bar S_{m,j+1/2}\bar U_{z,j+1/2}^{n+1}\right) \tag{24}$$

$$\frac{\bar{\mathbf B}_{\perp,j}^{n+1} - \bar{\mathbf B}_{\perp,j}^{n}}{\Delta\bar t} + \frac{(\bar V_z\bar{\mathbf B}_\perp)_{j+1/2}^{n+1} - (\bar V_z\bar{\mathbf B}_\perp)_{j-1/2}^{n+1}}{\Delta\bar z} + \frac{\bar{\mathbf V}_{\perp,j+1}^{n+1} - \bar{\mathbf V}_{\perp,j-1}^{n+1}}{2\Delta\bar z} = \frac{1}{4\bar\Omega_i\bar\Omega_e\Delta\bar z^2}\left(\frac{\bar\nu_{e,j+1}}{\bar n_{e,j+1}^{n+1}} - \frac{\bar\nu_{e,j-1}}{\bar n_{e,j-1}^{n+1}}\right) \cdot\left(\bar{\mathbf B}_{\perp,j+1}^{n+1} - \bar{\mathbf B}_{\perp,j-1}^{n+1}\right) + \frac{\bar\nu_{e,j}\left(\bar{\mathbf B}_{\perp,j+1}^{n+1} - 2\bar{\mathbf B}_{\perp,j}^{n+1} + \bar{\mathbf B}_{\perp,j-1}^{n+1}\right)}{\bar\Omega_i\bar\Omega_e\Delta\bar z^2\bar n_{e,j}^{n+1}} + \frac{\hat{\mathbf z}}{\bar\Omega_i\Delta\bar z^2\bar n_{e,j}^{n+1}} \cdot\left(\bar{\mathbf B}_{\perp,j+1}^{n+1} - 2\bar{\mathbf B}_{\perp,j}^{n+1} + \bar{\mathbf B}_{\perp,j-1}^{n+1}\right) - \frac{\left(\bar n_{e,j+1}^{n+1} - \bar n_{e,j-1}^{n+1}\right)}{4\bar\Omega_i\Delta\bar z^2(\bar n_{e,j}^{n+1})^2}\hat{\mathbf z}\times\left(\bar{\mathbf B}_{\perp,j+1}^{n+1} - \bar{\mathbf B}_{\perp,j-1}^{n+1}\right) \tag{25}$$

$$\frac{\bar p_j^{n+1} - \bar p_j^n}{\Delta\bar t} + \frac{(\bar V_z\bar p)_{j+1/2}^{n+1} - (\bar V_z\bar p)_{j-1/2}^{n+1}}{\Delta\bar z} + \frac{2\bar p_j^{n+1}\left(\bar V_{z,j+1/2}^{n+1} - \bar V_{z,j-1/2}^{n+1}\right)}{3\Delta\bar z} = \frac{1}{3}\bar\rho_j^{n+1}\bar\nu_{in,j} \cdot\left[\left(\bar{\mathbf V}_j^{n+1} - \bar{\mathbf U}_j^{n+1}\right)^2 + 2\xi\left(\frac{\bar p_{n,j}^{n+1}}{\bar\rho_{n,j}^{n+1}} - \frac{\bar p_j^{n+1}}{\bar\rho_j^{n+1}}\right)\right] - \frac{q_{j+1}^{n+1} - q_{j-1}^{n+1}}{3\Delta z} + \frac{2\bar\nu_{e,j}}{3\bar\Omega_e\bar\Omega_i\bar n_{e,j}^{n+1}}\left|\frac{\bar{\mathbf B}_{\perp,j+1}^{n+1} - \bar{\mathbf B}_{\perp,j-1}^{n+1}}{2\Delta\bar z}\right|^2 + \frac{2}{3}\bar Q_{p,j}^n \tag{26}$$

$$\frac{\bar p_{n,j}^{n+1} - \bar p_{n,j}^n}{\Delta\bar t} + \frac{(\bar U_z\bar p_n)_{j+1/2}^{n+1} - (\bar U_z\bar p_n)_{j-1/2}^{n+1}}{\Delta\bar z} + \frac{2\bar p_{n,j}^{n+1}\left(\bar U_{z,j+1/2}^{n+1} - \bar U_{z,j-1/2}^{n+1}\right)}{3\Delta\bar z} = \frac{1}{3}\alpha\bar\rho_j^{n+1}\bar\nu_{in,j} \cdot\left[\left(\bar{\mathbf V}_j^{n+1} - \bar{\mathbf U}_j^{n+1}\right)^2 - 2\xi\left(\frac{\bar p_{n,j}^{n+1}}{\bar\rho_{n,j}^{n+1}} - \frac{\bar p_j^{n+1}}{\bar\rho_j^{n+1}}\right)\right] - \frac{q_{n,j+1}^{n+1} - q_{n,j-1}^{n+1}}{3\Delta z} + \frac{2}{3}\left(\bar Q_{n,j}^n - \bar C_{n,j}\right) \tag{27}$$

where superscript $n+1$ represents the $(n+1)$th time step and subscript j is the spatial grid index, $\alpha = \rho_0/\rho_{n0}$ with the constants ρ_0 and ρ_{n0} being the plasma and neutral mass densities at the top boundary of the simulation domain, specified at the start of the simulation, and $\bar\nu_e = \bar\nu_{en} + \bar\nu_{ei}$. The variables with a bar in

(19)–(27) are those normalized to quantities at the top boundary. The normalization is $\bar{\rho} = \rho/\rho_0$, $\bar{\rho}_n = \rho_n/\rho_{n0}$, $\bar{\mathbf{V}} = \mathbf{V}/V_{A0}$, $\bar{\mathbf{U}} = \mathbf{U}/V_{A0}$, $\bar{\mathbf{B}} = \mathbf{B}/B_0$, $\bar{n}_e = n_e/n_{e0}$, $\bar{t} = t/t_0$, $\bar{z} = z/L$, $\bar{\Omega}_e = \Omega_{e0}t_0$, $\bar{\Omega}_i = \Omega_{i0}t_0$, $\bar{\nu}_{en} = \nu_{en}t_0$, $\bar{\nu}_{in} = \nu_{in}t_0$, $\bar{\nu}_{ei} = \nu_{ei}t_0$, $\bar{P} = P/\rho_0 V_{A0}^2$, $\bar{P}_n = P_n/\rho_{n0}V_{A0}^2$, $\bar{\mathbf{g}} = \mathbf{g}t_0/V_{A0}$, $\bar{S}_m = S_m t_0/\rho_0$, $\bar{L}_m = L_m t_0$, $\bar{Q}_p = Q_p t_0/\rho_0 V_{A0}^2$, $\bar{Q}_n = Q_n t_0/\rho_{n0}V_{A0}^2$, and $\bar{C}_n = C_n t_0/\rho_{n0}V_{A0}^2$. Here n_{e0} is the electron number density at the top boundary and determined at the start of the simulation, B_0 is the strength of the background magnetic field, $\Omega_{e0} = eB_0/m_e$, $\Omega_{i0} = eB_0/\bar{m}_{i0}$ with $\bar{m}_{i0}$ the average ion mass at the top boundary, $V_{A0} = B_0/(\rho_0\mu_0)^{1/2}$ is the Alfvén velocity at the top boundary with μ_0 the permeability in vacuum, and $t_0 = L/V_{A0}$ with L the length of the simulation domain.

The superscript and subscript are applied to every individual variable inside a pair of parenthesis in (19)–(27), e.g.,

$$\left(\bar{V}_z\bar{\rho}\bar{\mathbf{V}}_{\perp}^{n+1}\right)_{j+1/2} = \bar{V}_{z,j+1/2}^{n+1}\bar{\rho}_{j+1/2}^{n+1}\bar{\mathbf{V}}_{\perp,j+1/2}^{n+1} \tag{28}$$

where values at $j + 1/2$ are simply evaluated as the average of the values at two adjacent grids, e.g., $\bar{\rho}_{j+1/2} = (\bar{\rho}_{j+1} + \bar{\rho}_j)/2$ (note that $\bar{V}_z$ is defined at $j + 1/2$). The term $(\bar{V}_z^2\bar{\rho})_j$ in (22) (similar term in (24)) is evaluated with zip type differencing $(\bar{V}_z^2\bar{\rho})_j = \bar{\rho}_j\bar{V}_{z,j+1/2}\bar{V}_{z,j-1/2}$ to avoid certain nonlinear numerical instabilities [*Hirt*, 1968].

Equations (19)–(27) are a set of nonlinear algebraic equations, which can be cast into the concise form

$$\mathbf{f}\left(\mathbf{x}, \mathbf{x}^n, (n+1)\Delta t\right) = 0 \tag{29}$$

where $\mathbf{x}$ represents the (unknown) solution vector at time step $n+1$ and $\mathbf{x}^n$ the solution vector at time step n. At each time step, we use a Newton-like iterative method [e.g., *Kelley*, 2003] to solve the nonlinear algebraic equations (29) by using

$$\mathbf{x}_{k+1} = \mathbf{x}_k - \left[\mathbf{f}'\left(\mathbf{x}_k, \mathbf{x}^n, (n+1)\Delta t\right)\right]^{-1}\mathbf{f}\left(\mathbf{x}_k, \mathbf{x}^n, (n+1)\Delta t\right) \tag{30}$$

where subscript $k + 1$ (k) represents the $(k + 1)$th (kth) iteration and $[\mathbf{f}']^{-1}$ is the inverse of Jacobian matrix that has elements $J_{i,j} = \partial f_i/\partial x_j$ with f_i being the ith equation in function vector $\mathbf{f}$ and x_j the jth element of the solution vector $\mathbf{x}$. At each iteration, we solve a linear equation system (30) with a sparse matrix.

Solving the nonlinear system (29) of N equations is by no means easy when N is large because it is expensive to process a large Jacobian matrix at each iteration. Numerous methods have been developed to solve such a nonlinear equation system. Many are based on Krylov subspace (KSP) method [e.g., *Saad*, 2003], which is efficient for solving linear algebraic equations. In the present study, we adapt a nonlinear equation solver from a Portable Extensible Toolkit for Scientific Computation (PETSc) package developed by PETSc team at Argonne National Laboratory (URL:http://www.mcs.anl.gov/petsc). The scalable nonlinear equations solver (SNES) in the PETSc provides an efficient and extensible way of solving nonlinear equations based on Newton-like iterative method, which invokes one of various KSP-based algorithms to solve the linear equation system either sequentially or in parallel [*Balay et al.*, 1997].

4. Coupling Through MHD Waves

The most important effect included in the governing equations discussed in section 2.1, in contrast to the equations of conventional IT models, comes from the time-derivative terms in momentum equations and Faraday's law, with which the MHD wave propagation and reflection are included in a self-consistent manner. *Song et al.* [2009] and *Tu et al.* [2011] have, by numerically solving a subset of the above governing equations (i.e., without continuity and energy equations and without pressure gradients and gravity forces), investigated dynamic M-IT coupling when magnetospheric convection suddenly changes. Their simulations have shown that reflection of Alfvén waves in the ionosphere plays an important role in causing overshoots of ionospheric perturbations. In the following we present such overshoots and oscillations obtained from numerical solutions of the equations described in 2.1, to further illustrate M-I coupling through Alfvén waves. We also find some features that do not appear in solutions of the subset equations. With inclusion of the continuity and energy equations, compressional modes are present in the system.

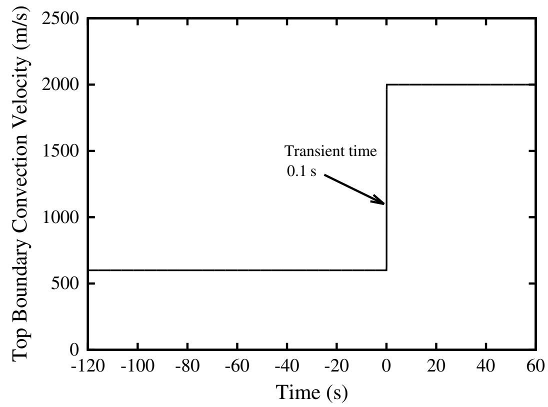

Figure 2. Time variation of antisunward convection velocity imposed at the top boundary.

4.1. Transients in the Ionosphere

The present simulation, with initial values and basic parameters specified as described above and spatial resolution $\Delta z = 5$ km, is carried out for the northern pole in winter solstice and at local midnight, background magnetic field $\mathbf{B}_0 = -B_0\hat{z}$ with $B_0 = 50,000$ nT, and initial (or background) plasma and neutral velocities set to 0. For the purpose of helping interpret the simulation results, we plot in Figure 1 altitude profiles of Alfvén speed $V_A = \sqrt{B_0/\rho\mu_0}$ and ion-neutral and electron collision frequencies, ν_{in} and $\nu_e = \nu_{en} + \nu_{ei}$, calculated at the start of the simulation. Note that the Alfvén speed changes with time since plasma mass density ρ does. The collision frequencies are held constant in time as are the production and loss rates because the density of individual neutral and ion species is not updated.

The modeled ionosphere/thermosphere system is driven by an antisunward convection velocity (along x direction) at the top boundary ($z = 1000$ km). The imposed V_x at the top boundary increases from 0 to 600 m/s in 0.1 s and is maintained at 600 m/s for 2 min; then, at the time taken as $t = 0$, it increases to 2000 m/s in 0.1 s and is maintained at this value for 1 min. The time history is shown in Figure 2. Since the time for the top boundary convection to increase from 600 m/s to 2000 m/s is 0.1 s, we use time step $\Delta t = 0.01$ s. Other time steps, such as 0.1 s and 1 s, have been tested. With larger time steps, fine variations are not resolved, but the essential features (overshoots and oscillations during the dynamic period) are the same as those from the simulation with the time step of 0.01 s. Note that the initial state of the ionosphere/thermosphere given by the IRI2011 and NRLMSISE00 models are not in equilibrium without the perturbation magnetic field and velocities. The first 2 min with weak convection velocity at the top boundary are run simply to establish equilibrium of the governing equations. The simulation of the time interval 0–60 s after establishment of equilibrium constitutes the real study of the dynamical response to the magnetospheric driver, which is presented and discussed below.

4.1.1. Wave Propagation, Reflection, and Overshoots

As mentioned already, overshoots and oscillations of ionospheric perturbations during the transient period are produced by superposition of incident and reflected waves. In order to clearly illustrate this point, we show in Figure 3 the altitude distribution of the antisunward plasma velocity V_x at selected times. At $t = 0$, the ionosphere is in a quasi steady state, established after a 2 min run from the initial ionosphere and thermosphere specified by empirical models. The velocity V_x has the value of 600 m/s (which has been imposed at the top boundary) uniformly at all altitudes down to 150 km; below about 150 km, where the ion-neutral collision frequency becomes higher than the ion gyrofrequency, the velocity decreases rapidly to the value of 0 imposed at the lower boundary. As the velocity at the top boundary is then increased to 2000 m/s over a short period of 0.1 s, the velocity change propagates downward along the field line, carried by Alfvénic perturbations, while collisions reduce the amplitude and neutral inertia loading reduces the propagation speed for lower frequency perturbations [*Song et al.*, 2005b]. At $t = 0.15$ s the wave front has reached 400 km altitude, with velocities at all higher altitudes increased above their initial quasi-steady value. At 0.46 s, equal to the Alfvén travel time in the present simulation, the wave front has arrived at the bottom of the ionosphere and the velocities have increased at all altitudes (with the exception of the collision-dominated region at the bottom). Later, at $t = 0.55$ s the velocities increase further at all altitudes and show slight enhancements in the region between about 150 and 300 km, consistent with in-phase superposition of incident and

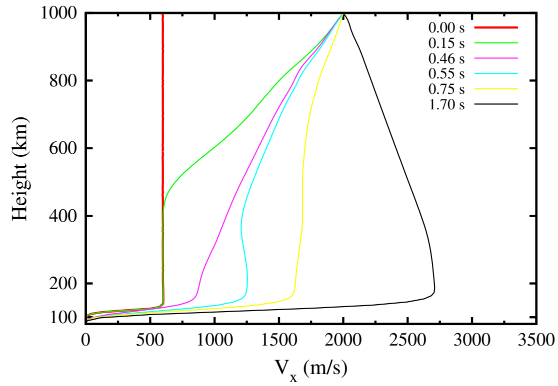

Figure 3. Altitude distribution of antisunward component of plasma velocity, V_x, at several given times.

reflected waves. Later still, at $t = 1.7$ s, strong overshoots (velocity value larger than that imposed at the top boundary) occur at all altitudes, due presumably to phase matching of incident and reflected waves.

Figure 4 displays contour plots of the x component (top) and y component (bottom) of plasma velocity as functions of time and altitude. The time is shown in units of Alfvén travel time, defined as the integrated time for a perturbation to propagate from the top to the bottom boundary at the local Alfvén speed, taking into account the variation of density with altitude; the actual propagation time is slightly (about 10%) longer than the nominal travel time calculated from the local Alfvén speed because of neutral inertia loading effect associated with strong collisions at the lowest altitudes [*Song et al.*, 2005b]. In the simulation the Alfvén travel time has the short value of about 0.46 s because the M-IT system has been scaled to a small size of only 920 km in altitude.

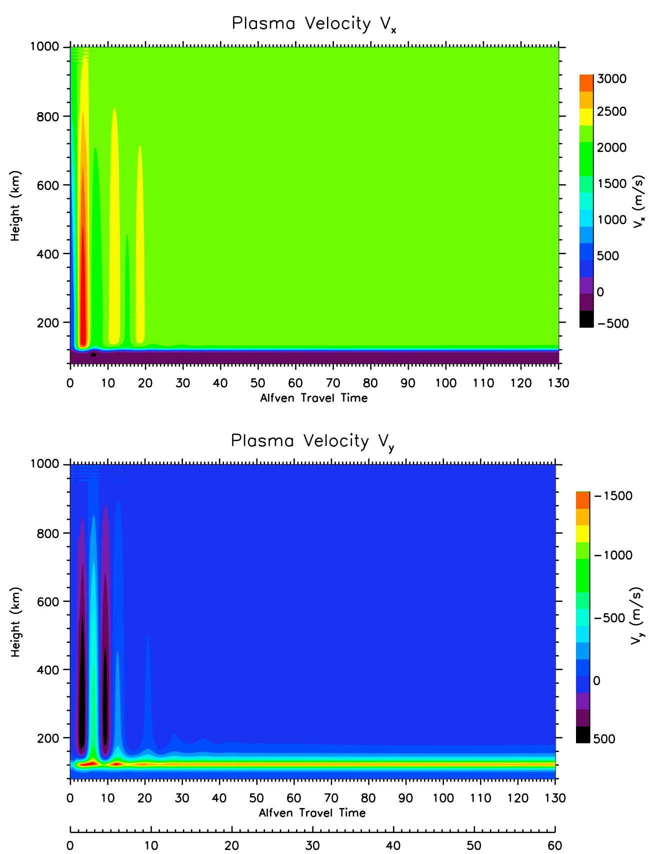

Figure 4. Plasma velocity components (top) V_x and (bottom) V_y as functions of time (in units of Alfvén travel time t_A) and altitude. The time is also given in seconds below the V_y panel.

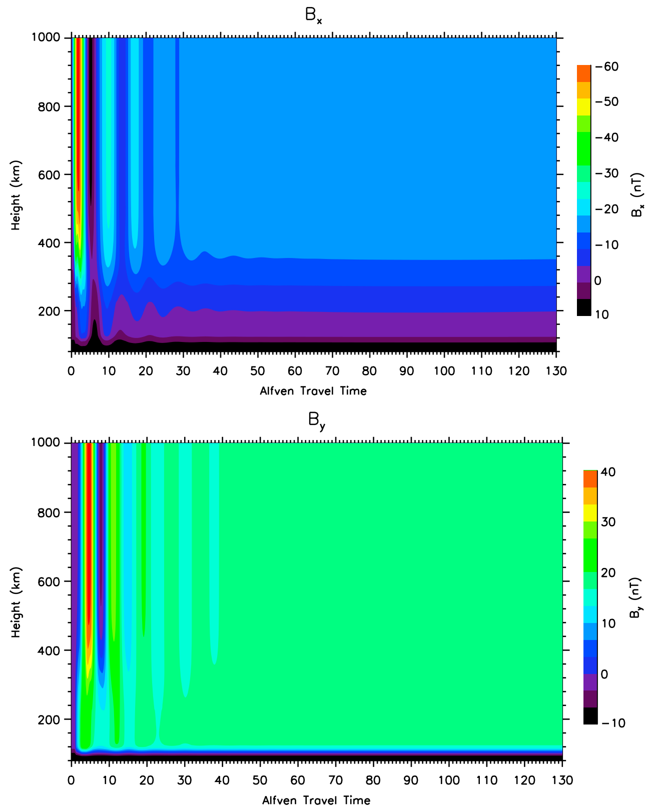

Figure 5. The *x* and *y* components of the perturbation magnetic field, B_x and B_y, as functions of Alfvén travel time and altitude.

As seen in Figure 4, the full strength of the driver reaches the bottom of the ionosphere in about 2 Alfvén travel times (about 1 s in the simulation). Afterward, V_x above 125 km first undergoes strong overshoots (1.5 times larger in magnitude than the velocity imposed at the top boundary), between $t = 2$ and $t = 4$ Alfvén travel times, and then in the region between about 130 km and 840 km is depressed below the velocity imposed at the top. Overshoot and depression repeat two more times. After $\sim$ 20 Alfvén travel times, V_x above 130 km has essentially reached a quasi steady state, with no significant altitude variation. Below 130 km, the velocities are much smaller, and there are weak oscillations remaining for a longer time. The fact that, at low altitudes, velocities take longer to reach steady state values and oscillations persist for a longer time can be accounted for by the much more frequent ion-neutral collisions there, as a consequence of which it takes longer to build up the Lorentz force (or equivalently the current) to balance the collision force [*Tu et al.*, 2011] and thus to establish the quasi steady state.

An interesting phenomenon shown already in the simulations of *Song et al.* [2009] and *Tu et al.* [2011] is that imposing antisunward convection velocity at the top boundary not only pushes the ionosphere to move in the antisunward direction but also produces a dawn-to-dusk component (positive for dawnward) of plasma flow (see Figure 4, bottom), owing to the *y* component of $\mathbf{J}\times\mathbf{B}$ force (Hall effect). This issue is further discussed in section 4.1.2.

Similar overshoots and oscillations are also observed in other ionospheric quantities and can be similarly explained as consequences of wave reflection. Figure 5 shows the B_x and B_y components of the magnetic field as functions of time and altitude. The magnetic field experiences strong variations during the first 40 Alfvén travel times and reaches a quasi steady state thereafter. The B_x is sunward and decreases with increasing altitude ($\partial B_x/\partial z < 0$), while B_y is dawnward and in general increases with increasing altitude (note the difference in dynamic range of the color coding for the two components). It can be shown, by examining the plasma momentum equation, that these spatial variations of the magnetic field are consistent with the variations of plasma velocity shown in Figure 4.

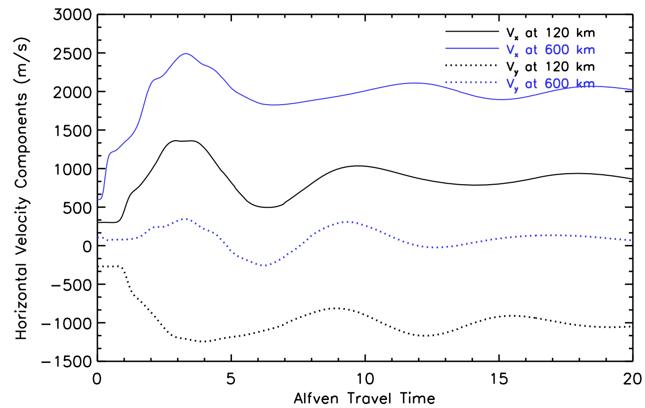

Figure 6. Time variations of V_x and V_y at 120 and 600 km during the first 20 Alfvén travel times.

4.1.2. The Dynamical Hall Effect

As shown in Figures 4 and 5, perturbations are induced in V_y and B_y even though the imposed velocity is in the x direction. Similarly to V_x, the V_y component also displays strong variations within the first 20 Alfvén travel times, but the magnitude of V_y is smaller than that of V_x. At altitudes below about 190 km, the variations last for a longer time than at higher altitudes. After about 40 Alfvén travel times, V_y subsides to near 0 above 160 km but remains strongly duskward around 120 km. This duskward velocity component is caused by the combined action of the y component of $\mathbf{J} \times \mathbf{B}$ force (or dawnward bending of field lines) and the difference in electron-neutral and ion-neutral collisions (the third term on the right-hand side of equation (3)), which are balanced by the ion-neutral collision force $\rho\nu_{in}(V_y - U_y)$ and by the spatial gradient of V_y once the plasma velocity has been established [*Song et al.*, 2009].

The presence in the lower ionosphere of velocity and magnetic field components perpendicular to the imposed magnetospheric convection velocity is well understood as the result of the Hall effect. Conventional M-I coupling models, however, derive this result from the steady state ionospheric Ohm's law with Hall and Pedersen conductivities and therefore have neglected all dynamical effects. This restriction is not present in our calculation, which uses the generalized Ohm's law (12) instead. The difference between the dynamical Hall effect and the conventional steady state Hall effect is most obvious from the appearance, during the transient phase in our simulation, of V_y and B_y perturbations at higher altitudes, where the ion-neutral collision frequency is low. In the conventional steady state description, the Hall effect produces V_y and B_y only in regions where the collision frequencies are high.

In order to better understand the dynamical Hall effect, we take a closer look at time variations of horizontal plasma velocity components. Shown in Figure 6 are time variations of V_x and V_y at two selected altitudes, 120 km and 600 km, during the first 20 Alfvén travel times, with particular attention to the change of velocity components from initial quasi-steady values at $t = 0$ during the first few Alfvén travel times. When the antisunward convection velocity imposed at the top boundary has jumped from 600 m/s to 2000 m/s during 0.1 s (about 1/5 of an Alfvén travel time), the induced perturbation propagates downward at high Alfvén speed (about 10,000 km/s at high altitudes but decreasing to under 3000 km/s in the F region). The resulting perturbation in V_x (an initial rapid increase) appears promptly at 600 km (see blue solid line in Figure 6) but with a delay of about 1 Alfvén travel time at 120 km (black solid line). The perturbation in V_y begins at 120 km (black dotted line) at almost the same time as the perturbation in V_x there and then appears at 600 km (blue dotted line) with a further delay of about 1 Alfvén travel time. This time sequence can be understood on the basis of the governing equations. When the imposed V_x propagates downward from the top boundary, it produces B_x self-consistently, according to the Walén relation; in this initial phase, from (3), perturbations in V_y and B_y are essentially negligible. After the wave front has reached the lower ionosphere, B_x begins to generate a B_y perturbation by the Hall effect through (10), (11), and (12). Note that wave reflection tends to increase the magnetic perturbation while decreasing the velocity perturbation above the reflection surface [*Song and Vasyliūnas*, 2013], and the decrease of electron density n_e below the F_2 peak amplifies the Hall term in (12). The perturbation in V_y is produced by B_y first in the low-altitude ionosphere, via the Lorentz force in (3), and is then carried upward by the reflected wave. This is the

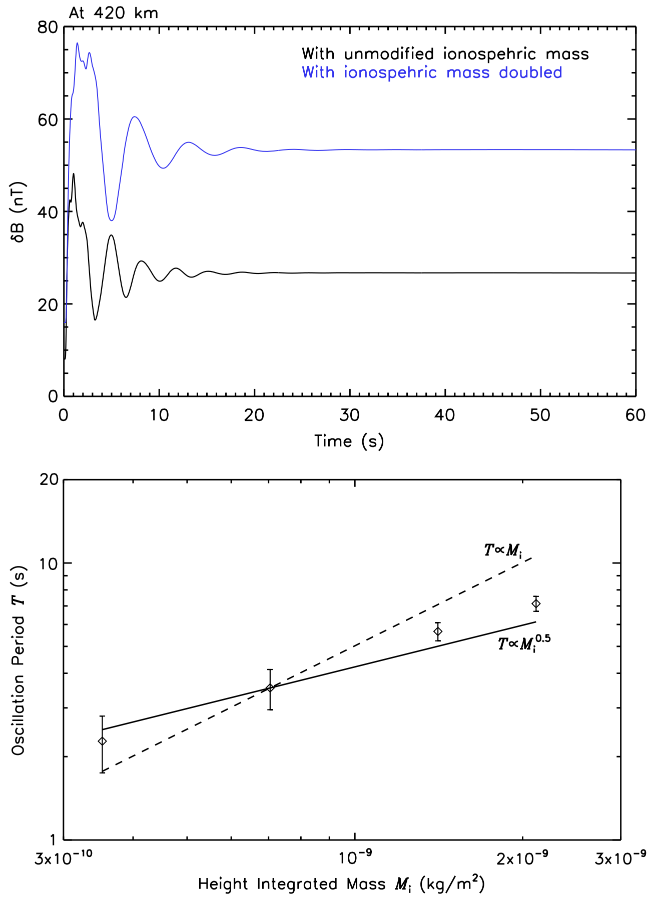

Figure 7. (top) Time variations in magnitude of the perturbation magnetic field $\delta B = (B_x^2 + B_y^2)^{1/2}$ at 420 km. Black line from simulation with unmodified initial ionospheric density, purple line from simulation with doubled initial ionospheric density. (bottom) Variation of oscillation period T versus height-integrated ionospheric mass M_i. Diamonds represent simulation results with half, unmodified, doubled, and tripled initial ionospheric mass density. Solid and dashed lines are the square root and linear dependence $T \propto M_i^{0.5}$ and $T \propto M_i$, respectively.

dynamical Hall effect plays in M-I coupling, a process not described by the conventional M-I coupling theory with its electrostatic assumption.

4.2. Dependence of Oscillation Period on Ionosphere/Thermosphere Inertia

The overshoots and damped oscillations shown in sections 4.1.1 and 4.1.2 suggest that the ionosphere/thermosphere act like a damped oscillator when it responds to a driving force from the magnetosphere. While it is natural to relate the damping to the dissipation of and work done by the Alfvén wave energy in the IT system, it is not obvious what exactly determines the oscillation period; the periods seen in Figures 4–6 do not equal the simple Alfvén travel time. This problem can be solved by carefully examining the dispersion relation derived from the governing equations in 2.1, which will be reported elsewhere. Here we compare simulations with different initial ionospheric densities, to see how the change affects the oscillation period.

We perform simulations with different initial densities of electron and individual ion species but maintain the same altitude profiles, the same neutral densities, and the same collision frequencies; the only change is in the height-integrated mass of the plasma. The results are shown in Figure 7 for simulations with half, unmodified, doubled, and tripled ionospheric mass density at the start of the simulations. Figure 7 (top) shows time variations in magnitude of the perturbation magnetic field $\delta B = (B_x^2 + B_y^2)^{1/2}$, for two simulations: one with unmodified ionospheric mass and one with doubled ionospheric mass. Doubling the initial ionospheric density (i.e., doubling the inertia) increases the oscillation period by a factor ~1.6. The dependence of the oscillation period on ionospheric inertia is demonstrated more clearly in Figure 7 (bottom), which shows that the oscillation period T varies approximately as a power of the height-integrated mass M_i, with

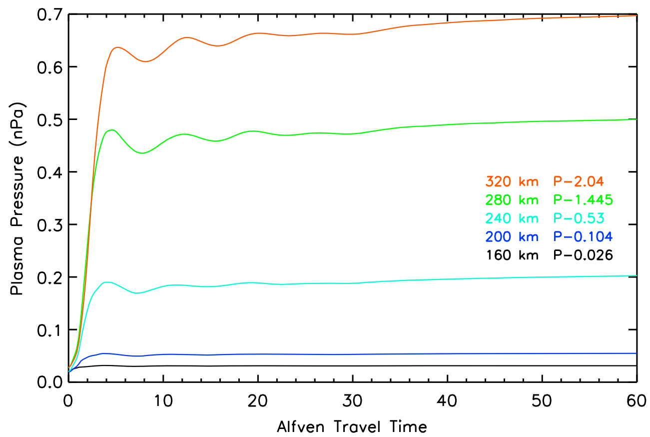

Figure 8. Time variations of plasma pressure at selected altitudes. Constant values have been subtracted from the pressure at each altitude to make the plot readable.

a power index slightly above 0.5. If the oscillation is related to multiple reflection of Alfvén waves up and down, the oscillation period is expected to be some multiple of the Alfvén travel time or proportional to $M_i^{0.5}$ (which is perhaps not inconsistent with the results of Figure 7, given the latter's uncertainties).

4.3. Excitation of Compressional Waves

The global response of the ionosphere/thermosphere, considered as a separate system, to a magnetospheric driver is conventionally often discussed in terms of penetration electric field [e.g., *Kelley et al.*, 1979; *Huang et al.*, 2008; *Tsurutani et al.*, 2008]. This concept may be useful sometimes as a mathematical description but not as a physical explanation because the electric field cannot directly drive large-scale motion [*Buneman*, 1992; *Vasyliūnas*, 2001; *Tu et al.*, 2008]. The simplest physical argument [*Vasyliūnas*, 2001, 2012] is that linear momentum in the electromagnetic field is very small compared to that in plasma bulk flow, so that it is the flow that imposes the electric field and not the other way around. The global ionosphere should be viewed as driven by, e.g., enhanced magnetospheric convection. The enhancement acts, at least initially, only on relatively small areas at high latitudes, which suggests the basic idea discussed by, e.g., *Song and Vasyliūnas*, [2013]: antisunward flow imposed in the open field line region (the polar cap) creates a higher pressure at the nightside interface to the closed field line region and a lower pressure at the dayside interface, launching fast mode compression and rarefaction waves, respectively, which by continuity produce convection cells in the polar ionosphere, from where they propagate, at the fast mode speed, into the low-latitude and equatorial ionosphere (producing equatorial upward motions, among other effects).

For propagation strictly along the magnetic field in low β plasma, MHD fast and Alfvén wave modes become identical, and the slow mode wave becomes essentially a sound wave. Since the restriction to parallel propagation is inherent in the geometry of our 1-D simulation, compression or rarefaction fast mode waves

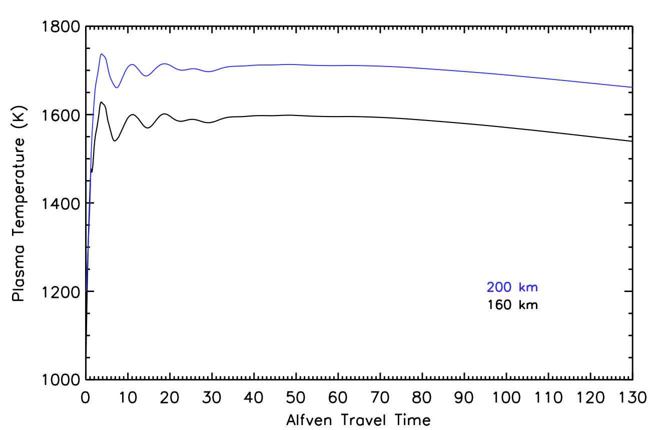

Figure 9. Time variations of plasma temperature at 160 and 200 km.

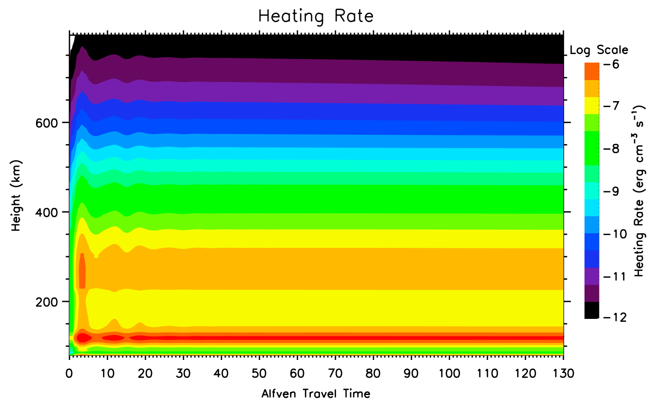

Figure 10. Contour plot of heating rate as a function of time and altitude.

cannot be directly investigated at present. To lowest order, equations (3) and (4) are not coupled, with (3) describing the Alfvén wave and (4) the sound wave. However, the presence of gravity in (4) couples pressure and gravity, producing an acoustic-gravity wave mode. Heating by oscillating Alfvén waves in the presence of ion-neutral collisions produces, through energy equation (7), a plasma thermal pressure oscillation which can propagate vertically up and down even in the 1-D simulation geometry. Figure 8 shows time variations of plasma pressure at selected altitudes of 160 km, 200 km, 240 km, 280 km, and 320 km. Oscillations of the pressure are evident, their amplitude increasing with increasing altitude, and there is a phase delay at higher altitudes, indicating a pressure wave propagating upward. The phase velocity can be estimated from the altitude dependence of the phase as 200 km/s or 400 km/s at lower or higher altitudes. These observed features are similar to those of acoustic-gravity waves in the atmosphere, but the propagation speed is much faster because of the different parameter range. Note also that the pressure oscillations at altitudes below about 200 km are almost in phase. As shown below in Figure 10, wave heating is concentrated around about 120 km and 275 km, giving two regions of strong heating that can drive pressure waves propagating up and down; in between the two, waves from the two sources propagate in opposite directions, thus making the phase delay at different altitudes essentially disappear.

Pressure oscillations are strongly associated with temperature variations. Figure 9 shows plasma temperature variations with time at two selected altitudes, which correspond to the variations seen in plasma pressure. The plasma temperature increases by 600–800 K because of frictional heating due to ion-neutral collisions. Figure 10 shows the contour plot of the heating rate (the sum of the first and second terms on the right-hand side of equation (7)) versus time and altitude. Large variations of the heating rate are seen during the first 20 Alfvén travel times, in association with large variations of plasma velocity (see Figure 3, noting that the relative velocity between plasma and neutrals corresponds essentially to the plasma velocity since the neutrals have not been appreciably accelerated). The strongest heating, producing a rapid increase of temperature, occurs when V_x overshoots the imposed convection velocity. The heating strength oscillates due to superposition of incident and reflected Alfvén waves, leading to oscillation of plasma temperature and hence of pressure.

5. Summary and Discussion

The simulation results reported in this paper clearly demonstrate the difference between the two descriptions of dynamic M-I coupling during the transient period when the IT system changes from one quasi steady state to another in response to an enhanced magnetospheric convection: our inductive-dynamic approach (in which inertia terms in the momentum equations are retained, Faraday's law and Ampère's law are included among the equations, and MHD wave effects are explicitly considered) with plasma/neutral dynamics and thermal dynamics incorporated, and the conventional steady state/electrostatic approach. While some previous studies included inductive effects within structure-resolved ionosphere, they either excluded plasma and neutral dynamics and/or thermal dynamics [e.g., *Hughes*, 1974; *Lysak*, 2004; *Lysak et al.*, 2013; *Woodroffe and Lysak*, 2012; *Streltsov and Lotko*, 2008] or interpret the simulation results in the context of conventional quasi steady state assumption [*Zhu et al.*, 2001; *Otto et al.*, 2003].

Overshoots and oscillations resembling those observed during substorms and other transient phenomena [e.g., *Russell and Ginskey*, 1993; *Bristow et al.*, 2003; *Huang et al.*, 2008] are clearly found in the simulations and can be explained by superposition of incident and reflected Alfvén waves, the phase difference between the two depending on altitude and time. The IT system responds as a damped oscillator. The damping can be understood by considering that the energy from the magnetosphere is dissipated (largely transferred to heat) and momentum from the magnetosphere does work (to push the IT). The oscillation period depends on the IT inertia because the force terms (associated with the current density in the momentum equations) are not proportional to the mass (unlike an ordinary pendulum). Note that this process is different from an Alfvén resonator [*Poliakov and Rapoport*, 1981], in which the Alfvén waves resonate between two altitudes (F layer peak and about 3000 km) where large Alfvén velocity gradients may exist.

We emphasize that the time of the dynamic stage should scale with the Alfvén travel time t_A over the real distance to the magnetopause or to the reconnection region in the magnetotail. As discussed in section 2.1, the simulations are conducted with a scaled M-IT system of only 920 km in altitude. If the simulation domain is extended out to the actual source of the driving force (e.g., at the dayside magnetopause), the Alfvén travel time will be of the order of 100 s and thus the dynamic stage will last 20–30 min. This scaling can be understood by considering Faraday's law and force balance in the plasma momentum equation, as discussed in more detail, e.g., by *Song and Vasyliūnas* [2013], who derive an order-of-magnitude estimate for the duration of change from one quasi steady state to another of $\sim 30\, t_A$ for typical high-latitude ionospheric parameters. The essential point is that the IT system must experience multiple reflections of Alfvén waves before reaching the quasi steady state, instead of just one transit of the wave from the top to the bottom boundary.

Detailed analysis of the simulation results also reveals the dynamical role that the Hall effect plays in the M-I coupling. The initial perturbation in V_x is carried downward by the incident Alfvén wave and produces the V_y perturbation first in the E region through the local Hall effect, the perturbation in V_y then being carried upward by the reflected wave. This is a dynamical process, critically dependent on M-I coupling via Alfvén waves; it is not included in conventional M-I coupling theory and models that neglect the inductive effects and also has no relation to the numerous studies [e.g., *Glaßmeier*, 1983; *Yoshikawa and Itonaga*, 2000; *Yoshikawa et al.*, 2011; *Fujii et al.*, 2011], based on conventional methods, of Hall current divergence at ionospheric altitudes.

Another interesting feature revealed by the simulations is plasma thermal pressure oscillation produced by Alfvén wave heating, which in the present 1-D geometry propagate with speeds of 200 km/s to 400 km/s along field lines. Such waves are similar to acoustic-gravity waves in the atmosphere, insofar as their amplitude and propagation speed both increase with altitude; they propagate, however, with much higher speed and are generated under different plasma conditions.

In the present study we have focused on physical understanding of the dynamic M-I coupling, making a number of simplifying assumptions (which perhaps make a detailed comparison of simulation results with observations somewhat premature). In particular, we have assumed a single fluid description for ions as well as time-invariant values for mean plasma particle mass and for photochemical production/loss rates and have adopted highly simplified treatments of heat conduction and photoelectron heating. Nevertheless, the overshoots and oscillations of the ionospheric perturbations revealed by the simulations resemble qualitatively (with shortened time scales) rather well those observed in the ionosphere during substorms and other transient phenomena [e.g., *Russell and Ginskey*, 1993; *Bristow et al.*, 2003; *Huang et al.*, 2008]. During a time interval of about 60 s, the plasma mass density barely changes (data not shown), suggesting that the assumptions of the constant mean plasma mass are valid for the time period considered; this is because the time scales of production/loss and transport are of the order of 100 s. When the simulation domain is extended to the magnetopause and the expected duration of the transient stage becomes tens of minutes, the assumption of time-constant mean particle mass and production/loss rates is no longer justifiable. It is then necessary to solve the multifluid equations for electrons and individual ion species to describe the IT system, which is a task for future development of the simulation model.

Acknowledgments
This study was supported by the NSF grants AGS-0903777 and AGS-1303596 and NASA grant NNX12AD22G to the University of Massachusetts Lowell. J. Tu thanks Jed Brown, Barry Smith, and Dmitry Karpeev at the Mathematics and Computer Science Division of Argonne National Laboratory for their valuable help in using the PETSc software package.

Robert Lysak thanks Akimasa Yoshikawa and an anonymous reviewer for their assistance in evaluating this paper.

References

Balay, S., W. D. Gropp, L. C. McInnes, and B. F. Smith (1997), Efficient management of parallelism in object oriented numerical software libraries, in *Modern Software Tools in Scientific Computing*, edited by E. Arge et al., pp. 163–202, Birkhäuser Press, Birkhäuser Boston, Mass.

Banks, P. M., and G. Kockarts (1973), *Aeronomy: Part B*, 355 pp., Academic Press, San Diego, Calif.

Bilitza, D., L.-A. McKinnell, M. B. W. Reinisch, and T. Fuller-Rowell (2011), The international reference ionosphere (IRI) today and in the future, *J. Geod.*, *85*, 909–920, doi:10.1007/s00190-010-0427-x.

Birk, G. T., and A. Otto (1996), A three-dimensional plasma-neutral gas-fluid code, *J. Comput. Phys.*, *125*, 513–525.

Bristow, W. A., G. Sofko, H. C. Stenbaek-Nielsen, S. Wei, D. Lummerzheim, and A. Otto (2003), Detailed analysis of substorm observations using SuperDARN, UVI, ground-based magnetometers, and all-sky imagers, *J. Geophys. Res.*, *108*(A3), 1124, doi:10.1029/2002JA009242.

Buneman, O. (1992), Internal dynamics of a plasma propelled across a magnetic field, *IEEE Trans. Plasma Sci.*, *20*, 672–677.

De Boer, J. D., J.-M. Noel, and J. P. St.-Maurice (2010), The effect of mesoscale regions of precipitation on the ionospheric dynamics, electrodynamics and electron density in the presence of strong ambient electric fields, *Ann. Geophys.*, *28*, 1345–1360.

Doe, R. A., J. F. Vickrey, and M. Mendillo (1995), Electrodynamic model for the formation of auroral ionospheric cavities, *J. Geophys. Res.*, *100*, 9683–9696.

Dreher, J. (1997), On the self-consistent description of dynamic magnetosphere-ionosphere coupling phenomena with resolved ionosphere, *J. Geophys. Res.*, *102*, 85–94.

Fedder, J. A., and J. G. Lyon (1995), The Earth's magnetosphere is 165 R_E long: Self-consistent currents, convection, magnetospheric structure, and processes for northward interplanetary magnetic field, *J. Geophys. Res.*, *100*, 3623–3635.

Fujii, R., O. Amm, A. Yoshikawa, A. Ieda, and H. Vanhamaki (2011), Reformulation and energy flow of the cowling channel, *J. Geophys. Res.*, *116*, A02305, doi:10.1029/2010JA015989.

Fuller-Rowell, T. J., D. Rees, S. Quegan, R. J. Moffett, M. V. Codrescu, and G. H. Millward (1996), A coupled thermosphere-ionosphere-plasmasphere model (CTIM), in *STEP Handbook on Ionospheric Models*, edited by R. W. Schunk and J. H. Allen, pp. 217–238, Utah State Univ., Logan, Utah.

Glaßmeier, K. H. (1983), Reflection of MHD-waves in the PC4–5 period range at ionospheres with non-uniform conductivity distributions, *Geophys. Res. Lett.*, *10*, 678–681.

Gombosi, T. I., D. L. DeZeeuw, C. P. Groth, K. G. Powell, and P. Song (1998), The length of the magnetotail for northward IMF: Results of 3D MHD simulations, in *Physics of Space Plasmas,* vol. 15, edited by T. Chang and J. R. Jasperse, pp. 121–128, MIT Press, Cambridge.

Hirt, C. W. (1968), Heuristic stability theory for finite-difference equations, *J. Comput. Phys.*, *2*, 339–355.

Huang, C.-S., K. Yumoto, S. Abe, and G. Sofko (2008), Low-latitude ionospheric electric and magnetic field disturbances in response to solar wind pressure enhancements, *J. Geophys. Res.*, *113*, A08314, doi:10.1029/2007JA012940.

Huba, J. D., G. Joyce, and J. A. Fedder (2000), Sami2 is another model of the ionosphere (SAMI2): A new low-latitude ionosphere model, *J. Geophys. Res.*, *105*, 23,035–23,053.

Hughes, W. J. (1974), The effect of the atmosphere and ionosphere on long period magnetospheric micropulsations, *Planet. Space Sci.*, *22*, 1157–1172.

Janhunen, P. (1996), Gumics-3: A global ionosphere-magnetosphere coupling simulation with high ionospheric resolution, in *Proceedings of ESA 1996 Symposium on Environment Modeling for Space-Based Applications, ESA,* vol. SP-392, pp. 233–239, ESTEC, Noordwijk, Netherland.

Kelley, C. T. (2003), *Solving Nonlinear Equations with Newton's Method*, 104 pp., SIAM, Philadelphia, Penn.

Kelley, M. C., B. G. Fejer, and C. A. Gonzales (1979), An explanation for anomalous ionospheric electric fields associated with a northward turning of the interplanetary magnetic field, *Geophys. Res. Lett.*, *6*(4), 301–304.

Kivelson, M. G., and D. J. Southwood (1988), Hydromagnetic waves and the ionosphere, *Geophys. Res. Lett.*, *15*, 1271–1274.

Lighthill, M. J. (1960), Studies on MHD waves and other anisotropic wave motion, *Philos. Trans. R. Soc.*, *252A*, 397–430.

Lysak, R. L. (1991), Feedback instability of the ionospheric resonant cavity, *J. Geophys. Res.*, *96*, 1553–1568.

Lysak, R. L. (2004), Magnetosphere-ionosphere coupling by Alfvén waves at midlatitudes, *J. Geophys. Res.*, *109*, A07201, doi:10.1029/2004JA010454.

Lysak, R. L., and C. Dum (1983), Dynamics of magnetosphere-ionosphere coupling including turbulent transport, *J. Geophys. Res.*, *88*, 365–380.

Lysak, R. L., and Y. Song (2002), Energetics of the ionospheric feedback interaction, *J. Geophys. Res.*, *107*(A8), 1160, doi:10.1029/2001JA000308.

Lysak, R. L., C. L. Waters, and M. D. Sciffer (2013), Modeling of the ionospheric Alfvén resonator in dipolar geometry, *J. Geophys. Res. Space Physics*, *118*, 1514–1528, doi:10.1002/jgra.50090.

Millward, G. H., R. J. Moffett, W. Quegan, and T. J. Fuller-Rowell (1996), A coupled thermospheric-ionospheric-plasmasphere model (CTIP), in *STEP: Handbook of Ionospheric Models*, edited by R. W. Schunk and J. H. Allen, pp. 239–279, Utah State Univ., Logan, Utah.

Otto, A., D. Lummerzheim, H. Zhu, O. Lie-Svendsen, M. H. Rees, and B. S. Lanchester (2003), Excitation of tall auroral rays by ohmic heating in field-aligned current filaments at F region heights, *J. Geophys. Res.*, *108*(A4), 8017, doi:10.1029/2002JA009423.

Picone, J. M., A. E. Hedin, D. Drob, and A. Aikin (2002), NRL-MSISE-00 empirical model of the atmosphere: Statistical comparisons and scientific issues, *J. Geophys. Res.*, *107*(A12), 1468, doi:10.1029/2002JA009430.

Poliakov, S. V., and V. O. Rapoport (1981), Ionospheric Alfvén resonator, *Geomag. Aeron.*, *21*, 610–614.

Raeder, J., J. Berchem, and M. Ashour-Abdalla (1998), The geospace environment modeling grand challenge: Results from a global geospace circulation model, *J. Geophys. Res.*, *103*, 14,787–14,797.

Richards, P., J. Fennelly, and D. Torr (1994), EUVAC: A solar EUV flux model for aeronomic calculations, *J. Geophys. Res.*, *99*, 8981–8992.

Richmond, A. D., E. C. Ridley, and R. G. Roble (1992), A thermosphere/ionosphere general circulation model with coupled electrodynamics, *Geophys. Res. Lett.*, *19*, 601–604.

Ridley, A. J., Y. Deng, and G. Toth (2006), The global ionosphere-thermosphere model, *J. Atmos. Sol. Terr. Phys.*, *68*, 839–864.

Russell, C. T., and M. Ginskey (1993), Sudden impulses at low latitudes: Transient response, *Geophys. Res. Lett*, *20*, 1015–1018.

Saad, Y. (2003), *Iterative Methods for Sparse Linear Systems,* 2nd ed., 447 pp., SIAM, Philadelphia, Penn.

Schunk, R. W. (2011), Ionosphere-thermosphere physics: Current status and problems (abstract), *AGU Chapman Conference on Modeling the Ionosphere/Thermosphere System*, Charleston, SC, 8-12 May.

Schunk, R. W., and A. F. Nagy (2000), *Ionospheres: Physics, Plasma Physics, and Chemistry*, 554 pp., Cambridge Univ. Press, New York.

Siscoe, G. L., N. U. Crooker, and K. D. Siebert (2002), Transpolar potential saturation: Roles of region 1 current system and solar wind ram pressure, *J. Geophys. Res.*, *107*(A10), 1321, doi:10.1029/2001JA009176.

Smith, F. L., and C. Smith (1972), Numerical evaluation of chapman's grazing incidence integral $ch(X, \chi)$, *J. Geophys. Res.*, *77*, 3592–3597.
Song, P., and V. M. Vasyliūnas (2013), Inductive-dynamic coupling of the ionosphere with the thermosphere and the magnetosphere, in *Modeling the Ionosphere-Thermosphere System, Geophys. Monogr. Ser., 201*, edited by J. Huba and R. W. Schunk, pp. 360, AGU, Washington, D. C.
Song, P., D. DeZeeuw, T. Gombosi, C. P. T. Groth, and K. G. Powell (1999), A numerical study of solar wind–magnetosphere interaction for northward interplanetary magnetic field, *J. Geophys. Res.*, *104*, 28,361–28,378.
Song, P., V. M. Vasyliūnas, and L. Ma (2005a), A three-fluid model of solar wind-magnetosphere-ionosphere-thermosphere coupling, in *Multiscale Coupling of Sun-Earth Processes*, edited by A. T. Y. Lui et al., pp. 447–456, Elsevier, Amsterdam, The Netherlands.
Song, P., V. M. Vasyliūnas, and L. Ma (2005b), Solar wind-magnetosphere-ionosphere coupling: Neutral atmosphere effects on signal propagation, *J. Geophys. Res.*, *110*, A09309, doi:10.1029/2005JA011139.
Song, P., V. M. Vasyliūnas, and X.-Z. Zhou (2009), Magnetosphere-ionosphere/thermosphere coupling: Self-consistent solutions for a one-dimensional stratified ionosphere in three-fluid theory, *J. Geophys. Res.*, *114*, A08213, doi:10.1029/JA013629.
Streltsov, A. V., and W. Lotko (2008), Coupling between density structures, electromagnetic waves and ionospheric feedback in the auroral zone, *J. Geophys. Res.*, *113*, A05212, doi:10.1029/2007JA012594.
Tsurutani, B. T., et al. (2008), Prompt penetration electric fields (PPEFs) and their ionospheric effects during the great magnetic storm of 30-31 October 2003, *J. Geophys. Res.*, *113*, A05311, doi:10.1029/2007JA012879.
Tu, J., P. Song, and B. W. Reinisch (2008), On the concept of penetration electric field, *AIP Conf. Proc.*, *974*, 81–85, doi:10.1063/1.2885036.
Tu, J., P. Song, and V. M. Vasyliunas (2011), Ionosphere/thermosphere heating determined from dynamic magnetosphere-ionosphere/thermosphere coupling, *J. Geophys. Res.*, *116*, A09311, doi:10.1029/2011JA016620.
Vasyliūnas, V. M. (2001), Electric field and plasma flow: What drives what?, *Geophys. Res. Lett.*, *28*, 2177–2180.
Vasyliūnas, V. M. (2012), The physical basis of ionospheric electrodynamics, *Ann. Geophys.*, *30*, 357–369, doi:10.5194/angeo-30-357-2012.
Vasyliūnas, V. M., and P. Song (2005), Meaning of ionospheric Joule heating, *J. Geophys. Res.*, *110*, A02301, doi:10.1029/2004JA010615.
Walker, R. J., T. Ogino, J. Raeder, and M. Ashour-Abdalla (1993), A global magnetohydrodynamic simulation of the magnetosphere when the interplanetary magnetic field is southward: The onset of magnetotail reconnection, *J. Geophys. Res.*, *98*(A10), 17,235–17,249.
White, W. W., G. L. Siscoe, G. M. Erickson, Z. Kaymaz, N. C. Maynard, K. D. Siebert, B. U. O. Sonnerup, and D. R. Weimer (1998), The magnetospheric sash and the cross-tail S, *Geophys. Res. Lett.*, *25*, 1605–1608.
Woodroffe, J. R., and R. L. Lysak (2012), Ultra-low frequency wave coupling in the ionospheric Alfvén resonator: Characteristics and implications for the interpretation of ground magnetic fields, *J. Geophys. Res.*, *117*, A03223, doi:10.1029/2011JA017057.
Yoshikawa, A., and M. Itonaga (2000), The nature of reflection and mode conversion of MHD waves in the inductive ionosphere: Multistep mode conversion between divergent and rotational electric fields, *J. Geophys. Res.*, *105*, 10,565–10,584.
Yoshikawa, A., A. Nakamizo, O. Amm, H. Vanhamaki, R. Fujii, Y.-M. Tanaka, T. Uozumi, K. Yumoto, and S. Ohtani (2011), Self-consistent formulation for the evolution of ionospheric conductances at the ionospheric E region within the M-I coupling scheme, *J. Geophys. Res.*, *116*, A09223, doi:10.1029/2011JA016449.
Zhu, H., A. Otto, D. Lummerzheim, M. H. Rees, and B. S. Lanchester (2001), Ionosphere-magnetosphere simulation of small-scale structure and dynamics, *J. Geophys. Res.*, *106*, 1795–1806.